Template-assisted synthesis of ultrathin graphene aerogels as bifunctional oxygen electrocatalysts for water splitting and alkaline/neutral zinc-air batteries

Qiang Li [a], Zhifang Sun [a], Chunyang Yin [a], Yang Chen [a], Dingjie Pan [b], Bingzhe Yu [b], Yi Zhang [a,*], Ting He [a,c,*], Shaowei Chen [b,*]

[a] Hunan Provincial Key Laboratory of Micro & Nano Materials Interface Science, College of Chemistry and Chemical Engineering, Central South University, 932 Lushan South Road, Yuelu District, Changsha, Hunan 410083, China
[b] Department of Chemistry and Biochemistry, University of California, 1156 High Street, Santa Cruz, CA 95064, USA
[c] School of Materials Science and Engineering, Xiangtan University, Xiangtan, Hunan 411105, China

ARTICLE INFO

ABSTRACT

Low-cost, high-performance oxygen catalysts are critical for electrochemical water splitting and metal-air batteries. Herein, carbon aerogels with skeletons consisting of few-layer graphene are derived pyrolytically from a hydrogel precursor using an array of NaCl crystals as the template, exhibiting a high electrical conductivity (869 S m^{-1}) and an ultralow mass density (11.1 mg cm^{-3}). The deposition of NiFe layered double hydroxide (NiFe-LDH) nanocolloids renders the aerogels active towards both the oxygen reduction/evolution reactions (ORR/OER), with the performances highly comparable to those of commercial benchmarks in both alkaline and neutral media. Results from operando Raman spectroscopy measurements and first principles caculations suggest that Fe(OH)$_3$ colloids facilitate the oxidation of Ni^{2+}, which lowers the energy barrier to 0.42 eV for OER, whereas the nitrogen-doped carbon aerogels are responsible for the ORR activity. With the composites used as bifunctional oxygen catalysts for electrochemical water splitting and rechargeable zinc-air batteries, the performances in both alkaline and neutral media are markedly better than those based on the mixture of commercial Pt/C and RuO$_2$. Results from this study highlight the unique advantages of ultrathin graphene aerogels in the development of effective catalysts for electrochemical energy devices.

1. Introduction

With the rapid exhaustion of fossil fuels and the rise in environmental awareness, development of new technologies for the storage and use of sustainable clean energy has been attracting attention worldwide. Rechargeable zinc-air battery (ZAB) has emerged as a promising solution in view of the high energy density, low cost, safe operation conditions and resource sustainability [1]. Yet, the energy efficiency of rechargeable ZAB is typically under 55 % at the specific capacity of 0.5 to 2 mAh cm^{-2} [2–4], far below the threshold of 11.7 mAh cm^{-2} needed to be competitive with Li-ion cells (specific energy density 100 Wh kg^{-1}) [5,6]. This is mainly due to the lack of satisfactory bifunctional oxygen catalysts towards both the oxygen reduction/evolution reactions (ORR/

OER). In addition, production of hydrogen via electrochemical water splitting is also a viable strategy [7]. Yet, in water electrolyzers, the efficiency of the hydrogen evolution reaction (HER) at the cathode can be severely compromised by the sluggish electron-transfer kinetics of OER at the anode [8,9]. Therefore, it is of both fundamental and technological significance to develop high-performance, low-cost, and scalable advanced oxygen electrocatalysts for ORR and OER.

It is well-known that the activity of the oxygen electrocatalysts depends greatly on the extent of active site utilization [3,10,11], and three-dimensional (3D) carbon aerogels have been attracting particular interest, primarily because of the ready accessibility of the catalytic active sites and abundant channels for efficient mass transfer of reactant species and electrolyte ions [7,12,13]. Thus, one can envisage that the

---

structure of the carbon skeletons plays a critical role in determining the ORR and OER performances. For a monolayer graphene, the surface area can be as high as 2630 m^2 g^{-1} [14]. Therefore, to maximize the accessible surface area of the carbon aerogels, ultrathin graphene walls are preferred for the skeletons. Yet, too thin the graphene layers may compromise the mechanical strength and hence structural integrity of the carbon framework [15]. Thus, careful structural engineering is needed to strike a good balance between the carbon skeleton thickness and materials performance. This can be achieved with carbon aerogels consisting of few-layer graphene in the structural framework. Currently, graphene aerogels are mostly prepared by chemical vapor deposition (CVD) where graphene is deposited onto select supporting substrates (e. g., metal foams) [16], and self-assembly of graphene oxide (GO) nanosheets via gel-sol [17], freeze casting [18], foam coating [19], spray discharge [20], etc. The former requires rather sophisticated instrumentation and hash conditions, while the latter generally exhibits only nonideal conductivity due to the presence of functional groups and thick layers of GO [21]. To our knowledge, despite the progress, it remains a formidable challenge to construc carbon aerogels with few-layer graphene that feature an interconnected 3D structure and high electrical conductivity, critical characteristics needed to facilitate the electrocatalytic reactions [22,23].

Another important factor that dictates the electrocatalytic performance is the intrinsic activity of the active sites. Active sites of single species are unlikely to exhibit high performance simultaneously for diverse reactions (e.g., ORR and OER), as demonstrated in theoretical and experimental studies [3,6,24–26]. For instance, carbon-based materials can act as effective ORR catalysts when deliberately doped with select metal and nonmetal heteroatoms (e.g., N, P, B, Fe, Co, etc), due to manipulation of the electronic structure and the formation of rich edge defects [27–30]; whereas NiFe (oxy)hydroxides are known to be effective towards OER, although the mechanism remains controversial, and the activity can be impacted by the stacking and undesirable electrical conductivity of the metal (oxy)hydroxide [31–35]. Bifunctional oxygen electrocatalsyts can therefore be constructed by integrating these materials into advanced nanocomposites for both ORR and OER [36–39]. Yet, the performance thus far has remained below the level required for rechargeable ZAB and water electrolyzers.

In the present study, we describe a buttom-up stratgy for the fabrication of ultrathin carbon aerogels consisting of few-layer graphene in the skeletons loaded with NiFe layered double hydroxide (NiFe-LDH) colloids. The carbon aerogels are prepared by controlled pyrolysis of a gelatin hydrogel precursor using arrays of NaCl crystals as the sacrificial template [40,41]. NiFe-LDH colloids are then adsorbed onto the aerogel surface. The nanocomposites exhibit high electrical conductivity (up to 869 S m^{-1}) and remarkable electrocatalytic activity towards both ORR and OER in alkaline/neutral media, markedly better than those of commercial precious metal-based benchmarks. The pyridinic/graphitic N dopants, edge defects, and oxygen vacancies are collectively responsible for the ORR activity, while the NiFe-LDH functions as the active sites for OER, where the surface-adsorbed Fe(OH)$_3$ colloids facilitate the oxidation of Ni^{2+}, likely due to the electron delocalization effect (modified electronic structure). Density functional theory (DFT) calculations further reveal that the Fe(OH)$_3$ colloids enhance the performance of NiFe-LDH for OER by modulating the formation of reaction intermediates and lowering the energy barrier of key reaction steps. The best sample exhibits an ultralow potential difference (ΔE) of only 0.61 V between the ORR half-wave potential (E$_{1/2}$) and the OER potential (E$_{OER,10}$) needed to reach the current density of 10 mA cm^{-2}, and can be used as effective bifunctional oxygen electrocatalysts in water splitting and rechargeable liquid/flexible alkaline and liquid neutral ZABs.

2. Results and discussion

2.1. Sample synthesis and structural characterization

The synthetic procedure for the ultrathin carbon aerogels includes two major steps (Scheme 1). Experimentally, arrays of cubic NaCl crystals were used as the structural template [40], and the confined space between the NaCl crystals was filled with a gelatin hydrogel. Subsequent thermal annealing at elevated temperatures, followed by removal of the NaCl templates by water, led to the formation of ultrathin carbon aerogels consisting of few-layer graphene, which were denoted as GA$_x$ with x representing the NaCl concentrations (i.e., 0, 0.09 and 0.18 g mL^{-1}). NiFe-LDH colloids were then adsorbed onto the carbon scaffold by immersing the aerogels into a NiFe-LDH solution [42]. The obtained composites were referred to as (NiFe-LDH)$_n$/GA$_x$ with n = 1, 2, and 3 signifying the loadings of the NiFe-LDH colloids at 14.7 wt%, 1.7 wt%, and 0.2 wt%, respectively. The experimental details are included in the Supporting Information.

The morphologies and microstructures of the nanocomposites were first investigated by scanning electron microscopy (SEM) and transmission electron microscopy (TEM) measurements. As shown in Fig. S1a-b, in the absence of the NaCl crystal template, the GA$_0$ sample shows a macroporous structure (pore diameter ca. 20 μm) and a thick wall of at least 1 μm. By contrast, the introduction of the NaCl crystal templates led to the formation of much denser and smaller pores (pore diameter under 1 μm), as observed with GA$_{0.09}$ (Fig. S1c-d) and GA$_{0.18}$ (Fig. S1e-f), where the cavities largely retained the cubic shape and dimension of the original NaCl crystals with an ultrathin wall, most likely due to the spatial confinement of the gelatin hydrogel precursor between the NaCl crystals. In fact, the thickness of the carbon skeletons varied in the orders of GA$_0$ (>1 μm) > GA$_{0.09}$ (1 ~ 100 nm) > GA$_{0.18}$ (<5 nm).

Notably, as compared to the smooth surface of GA$_{0.18}$ (Fig. 1a-b, and S1e), one can see a number of nanoparticles on the surface of (NiFe-LDH)$_1$/GA$_{0.18}$ (Fig. 1c), demonstrating the successful adsorption of the NiFe-LDH colloids onto the aerogel surface. Note that the NaCl crystals can be easily removed by ultrapure water (Fig. S1e-f). From the TEM image in Fig. 1d, one can see that the sample consists of extensive cavities of ca. 15 nm in diameter (red dashed circles), consistent with the residual cubic NaCl crystals of 10 ~ 20 nm (Fig. S1f). In high-resolution TEM measurements (Fig. 1e), (NiFe-LDH)$_1$/GA$_{0.18}$ can be seen to exhibit well-defined lattice fringes, with an interplanar distance of 0.23 nm (box I) and 0.38 nm (box III), due to the (0 0 2) facets of Ni(OH)$_2$ and (0 2 0) facets of Fe(OH)$_3$ colloids, respectively, whereas box II is mostly amorphous due to the NiFe-LDH colloids, as manifested in the inverse fast Fourier transform (IFFT) patterns shown in the inset [9,43,44]. That is, the (NiFe-LDH)$_1$/GA$_{0.18}$ nanocomposite consisted of nanocrystalline Fe(OH)$_3$ colloids adsorbed onto the NiFe-LDH surface. Elemental mapping analysis based on energy-dispersive X-ray spectroscopic (EDS) measurements (Fig. 1f) shows that both C and N were distributed homogeneously throughout the entire sample, suggesting successful carbonization of the hydrogel precursor and uniform doping of N into the carbon scaffold. In addition, one can see a rather consistent, but discrete distribution pattern of the Ni, Fe and O elements, due to the deposition of NiFe-LDH nanocolloids onto the carbon surface.

In topographic measurements by atomic force microscopy (AFM), the GA$_{0.18}$ sample can be seen to indeed exhibit a 2D nanosheet morphology (Fig. 1g and S1g), with a uniform thickness of ca. 1.07 nm, corresponding to about 3 graphene layers [45]. This is markedly thinner than leading results reported with relevant graphene derivatives, such as graphene derived from phytic acid (2.5 nm) [46], reduced graphene oxide (rGO, 2 ~ 4 nm) [21,47], and even commercially available graphene samples (ca. 1.4 nm, by CVD) [45]. Remarkably, the GA$_{0.18}$ aerogel exhibits an ultralow mass density of only 11.1 mg cm^{-3}, and can be easily produced in a large yield (Fig. S2). In fact, a red peach blossom flower can easily bear the weight of a piece of the carbon aerogel (ca.
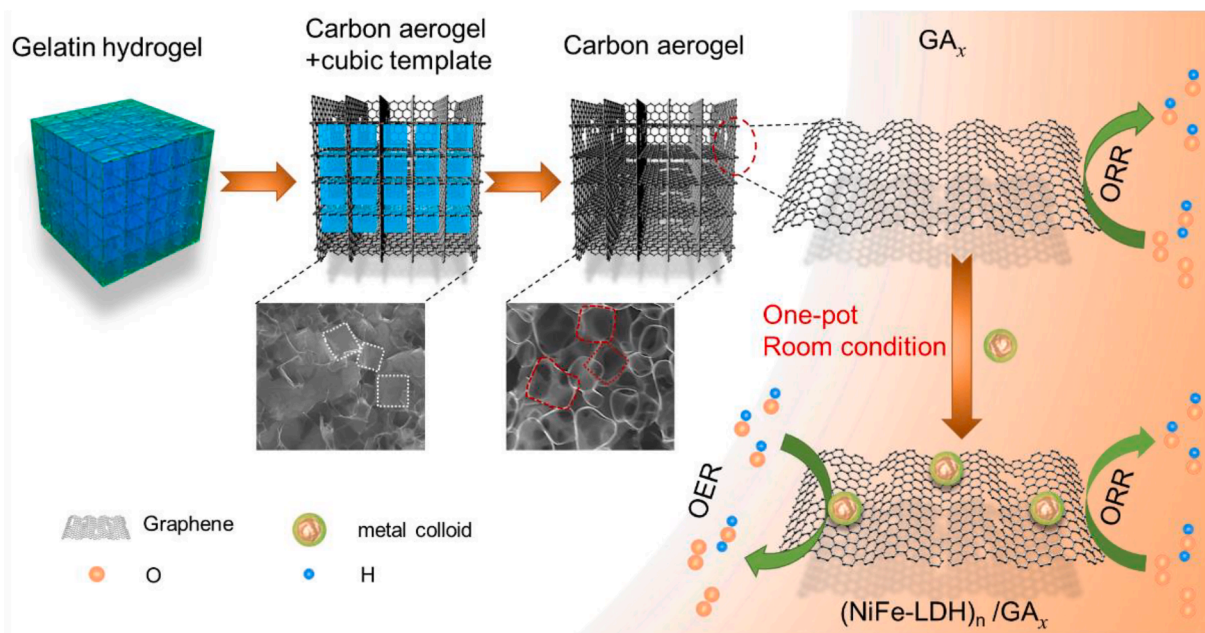
Scheme 1. Schematic illustration of the synthesis of ultrathin carbon aerogel (NiFe-LDH)$_n$/GA$_x$.

8.7 cm^3) without any deformation of its petals (Fig. 1**h**).

The porosity of the samples was then examined in nitrogen sorption measurements, where the Brunauer–Emmett–Teller (BET) specific surface area was estimated to be 226.9 m^2 g^{-1} for the template-free GA$_0$ sample, and increased substantially to 344.3 m^2 g^{-1} for GA$_{0.09}$, and 328.1 m^2 g^{-1} for GA$_{0.18}$ (Fig. 2**a**). Note that both GA$_{0.09}$ and GA$_{0.18}$ show a similar pore size, including micropores and macropores (up to 20 nm), whereas GA$_0$ consists only of micropores (<2 nm) (Fig. 2**b**). Further structural insights were obtained in Raman measurements (Fig. 2**c**), where all samples exhibited a well-defined D band at 1354 cm^{-1} and G band at 1587 cm^{-1}, with a very close intensity ratio (I$_D$/I$_G$) of ca. 0.96, suggesting a similarly graphitized structure in the GA$_x$ samples. The broad peak within the range of 2600 to 2900 cm^{-1} is likely the combined contributions of the D + D' and 2D bands, confirming the formation of structural defects within the carbon scaffolds [48].

Remarkably, despite the ultrathin skeletons, the resultant GA$_x$ samples exhibited a high specific conductivity (σ/ρ) [49], as manifested in four-probe measurements. Notably, the specific conductivity was found to increase with increasing pressure (Fig. S3**a**) and vary among the samples. In fact, the electrical conductivity (σ) at 30 MPa increased in the order of GA$_0$ (98.7 S m^{-1}) < GA$_{0.09}$ (290.2 S m^{-1}) < GA$_{0.18}$ (869.4 S m^{-1}) (Fig. 2**d**). Note that such conductivity is markedly higher than that of a number of graphene and rGO aerogels reported previously [49]. A similar trend was observed by mixing the GA$_x$ samples with a PTFE binder, GA$_0$ (0.02 S m^{-1}) < GA$_{0.09}$ (12.29 S m^{-1}) < GA$_{0.18}$ (34.89 S m^{-1}) (Fig. 2**e**). The corresponding X-ray diffraction (XRD) patterns are shown in Fig. 2**f and S3b-c**. All samples can be seen to exhibit two major diffraction peaks at 2θ ≈ 25° and 44°, due to the (0 0 2) and (1 0 1) crystalline facets of graphitic carbon (JCPDS PDF#00–041-1487) [50], and additional patterns of the NiFe-LDH colloids can be identified with the (NiFe-LDH)$_1$/GA$_{0.18}$ composites at 2θ ≈ 28.5°, 37.3°, 41.2°, and 41.8°, consistent with those of Ni(OH)$_2$ colloidal particles (Ni colloids), Fe(OH)$_3$ colloidal particles (Fe colloids), and NiFe-LDH colloids, further confirming the successful deposition of these metal colloids onto the GA surface (along with a trace amount of KCl and KNO$_3$ impurities). Yet, the features were much broadened, due to the small size and/or amorphous phase [51], in good agreement with results from the TEM measurements.

The elemental composition and valency of the samples were then examined by X-ray photoelectron spectroscopy (XPS) measurements. In the C 1 s spectra (Fig. S4**a**), the sp^2 C and C—N peaks can be readily resolved in all GA$_x$ samples, indicating successful graphitization of the hydrogel precursors and doping of N into the resulting carbon skeletons (consistent results were obtained with the (NiFe-LDH)/GA$_x$ composites, Fig. S5**a**) [52]. In the corresponding N 1 s spectra (Fig. 2**g**), the pyridinic N, pyrrolic N, graphitic N, and oxidized N can be deconvoluted at 398.5, 400.0, 401.0, and 402.9 eV, respectively [53]. On the basis of the integrated peak areas, the contents of pyridinic N and graphitic N were estimated to be 2.0 at% and 2.4 at% for GA$_{0.18}$, respectively, which are comparable with those for GA$_{0.09}$ (1.7 at%, 2.4 at%) and GA$_0$ (1.2 at%, 1.6 at%) (Table S1-S2). In the O 1 s spectra (Fig. S4**b, S5b**, and Table S3), the metal-O species can be readily identified in (NiFe-LDH)$_1$GA$_{0.18}$, but absent in the metal-free GA$_x$ samples [7].

From Fig. 2**h,** the Ni 2p electrons of (NiFe-LDH)$_1$/GA$_{0.18}$ can be seen to consist of two doublets at 855.2/872.9 and 856.5/874.3 eV, corresponding respectively to the 2p$_{3/2}$/2p$_{1/2}$ electrons of Ni^{2+} and Ni^{3+} [4,54], at 20 % Ni^{2+} and 80 % Ni^{3+}, whereas only Ni^{2+} was identified in Ni colloids (855.1/872.8 eV) [55]. In the Fe 2p spectra (Fig. 2**i**), the Fe^{2+} and Fe^{3+} species can be deconvoluted from both (NiFe-LDH)$_1$/GA$_{0.18}$ and Fe colloids [56,57], with the 2p$_{3/2}$/2p$_{1/2}$ doublet at 710.1/723.4 and 712.2/725.2 eV for (NiFe-LDH)$_1$/GA$_{0.18}$ and 710.0/723.6 and 712.0/725.4 eV for Fe colloids, respectively, corresponding to a Fe^{3+}/(Fe^{2+} + Fe^{3+}) ratio of 59 % and 88 % (the dashed curves in (i) are for the Ni LMN spectra [58]). In comparison to the monometallic Ni and Fe colloids alone, the Ni and Fe binding energies in (NiFe-LDH)$_1$/GA$_{0.18}$ can be seen to exhibit a positive and negative shift, respectively, suggesting effective electron transfer from Ni^{2+} to Fe^{3+} in (NiFe-LDH)$_1$/GA$_{0.18}$ [4,11]. It has been known that electron-deficient nickel centers are critical in the formation of key OER intermediates (O* and OO*), while the electron-rich Fe^{3+} sites facilitate OER by lowering the energy barrier from OH* to O* [59]. Such synergistic interactions between Fe^{3+} and Ni^{2+} in (NiFe-LDH)$_1$/GA$_{0.18}$ are most likely responsible for the enhanced the OER activity, as observed below. Note that the atomic ratio of Ni (3.1 at%) to Fe (3.0 at%) is close to 1:1 in (NiFe-LDH)$_1$/GA$_{0.18}$ (Table S1), in accord with the initial feed ratio in sample preparation.

2.2. Electrocatalytic activity

The ORR performances of the GA composites (free of metal colloids) were first evaluated via the cyclic voltammetry (CV) tests. From Fig. 3**a**
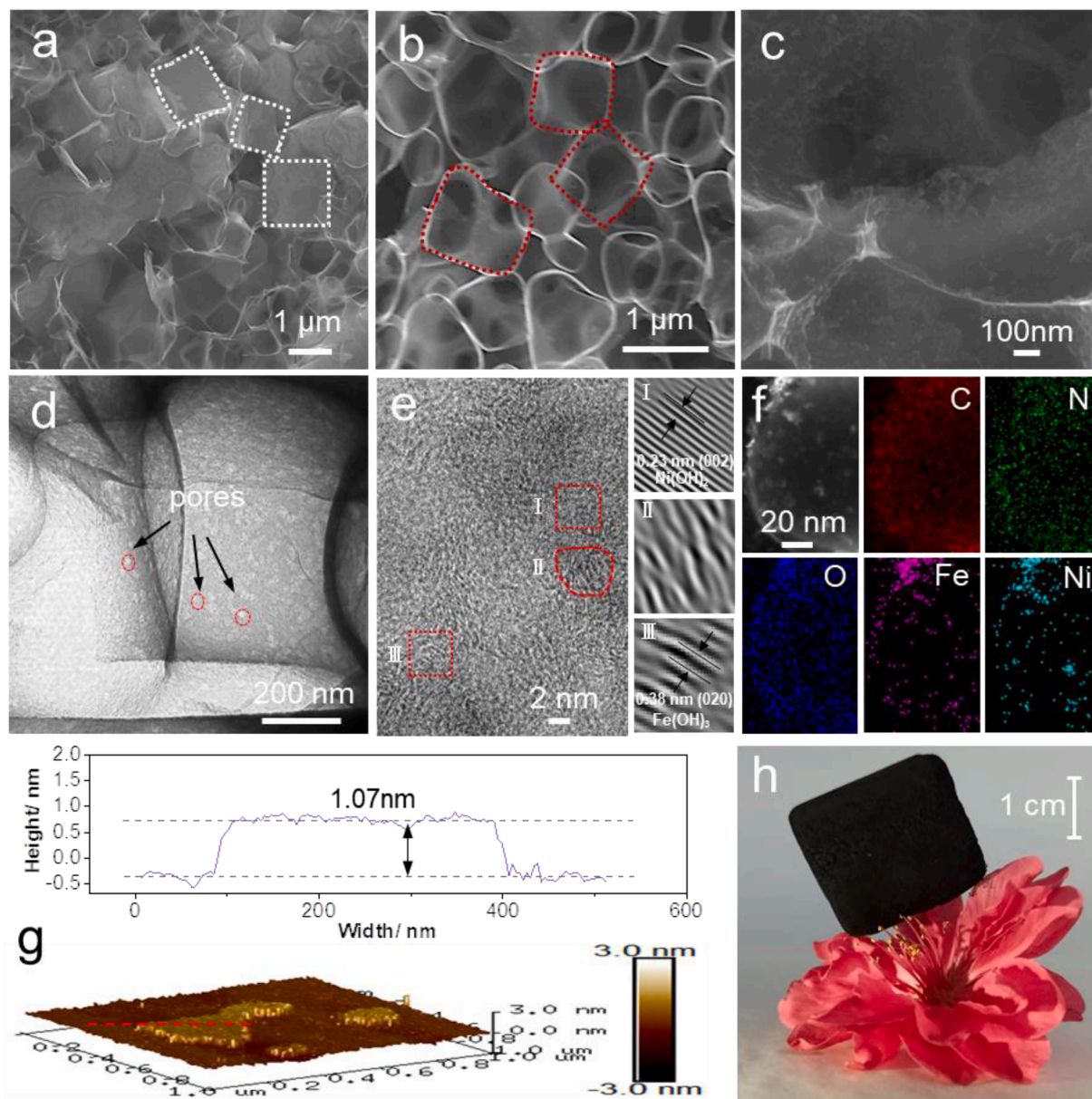
Fig. 1. SEM images of $GA_{0.18}$ (a) before and (b) after the removal of the NaCl crystal template by water. (c) SEM image of $(NiFe-LDH)_1/GA_{0.18}$. (d) TEM image of $GA_{0.18}$. (e) HRTEM image of $(NiF-LDH)_1/GA_{0.18}$ and the corresponding IFFT images of three regions. (f) HAADF-STEM image of $(NiF-LDH)_1/GA_{0.18}$ and the corresponding EDS elemental maps. (g) AFM topograph (bottom) and z-scan profile (top) of $GA_{0.18}$. (h) Photograph of a piece of $GA_{0.18}$ (ca. 8.7 cm^3) supported on a peach blossom flower.

and S6a, one can see that in contrast to the featureless responses in N_2-saturated 0.1 M KOH (dotted curves), GA_x, $(NiFe-LDH)_1/GA_{0.18}$ and commercial 20 wt% Pt/C all showed a well-defined voltammetric peak when the solution was purged with O_2 (solid curves), suggesting effective ORR activity of the samples. Notably, $GA_{0.18}$ exhibits the most positive peak potential ($E_p = +0.791$ V) among the metal-free sample series, which was only 25 mV more negative than that of Pt/C (+0.816 V), and with the deposition of NiFe-LDH, E_p remained virtually unchanged at + 0.796 V with $(NiFe-LDH)_1/GA_{0.18}$, as NiFe-LDH colloids alone displayed no ORR activity (Fig. S6c). That is, the ORR activity of $(NiFe-LDH)_1/GA_{0.18}$ is primarily due to the GA scaffolds.

Consistent results were obtained in linear sweep voltammetry (LSV) measurements with a rotating disk electrode (RDE) (Fig. 3b), where $GA_{0.18}$ displays a more positive half-wave potential ($E_{1/2} = +0.840$ V) than other GA_x samples and even commercial 20 wt% Pt/C (+0.831 V), and the performance remained practically unaffected by the deposition

of NiFe-LDH (Fig. S6c). Note that the performance of $GA_{0.18}$ ($E_{1/2} = +0.840$ V and onset potential $E_{onset} = +0.976$ V) actually represents a record for graphene-based metal-free ORR catalysts (Fig. 3c, Table S4). This is most likely facilitated by the excellent electrical conductivity and highly exposed and available defect sites of the carbon aerogels, as compared to other GA_x samples (Fig. 2), as both the N dopants and edge defects have been recognized as the active sites for ORR via regulating the electronic structure of adjacent C atoms [60,61].

The corresponding Tafel slope can be estimated to be 79 mV dec^{-1} for $GA_{0.18}$ and 78 mV dec^{-1} for $(NiFe-LDH)_1/GA_{0.18}$, as compared to 82 mV dec^{-1} for commercial Pt/C (Fig. S7a), indicating a fast electron-transfer kinetics process. The average electron-transfer number (n) and H_2O_2 yield were calculated to be 3.87 and 6.4 % for $GA_{0.18}$, which are comparable to those of Pt/C (3.88 and 5.4 %), suggesting a dominant four-electron pathway for ORR (Fig. S7b). $GA_{0.18}$ also exhibits remarkable durability (Fig. S7c) with a negative shift of $E_{1/2}$ by only 8 mV after
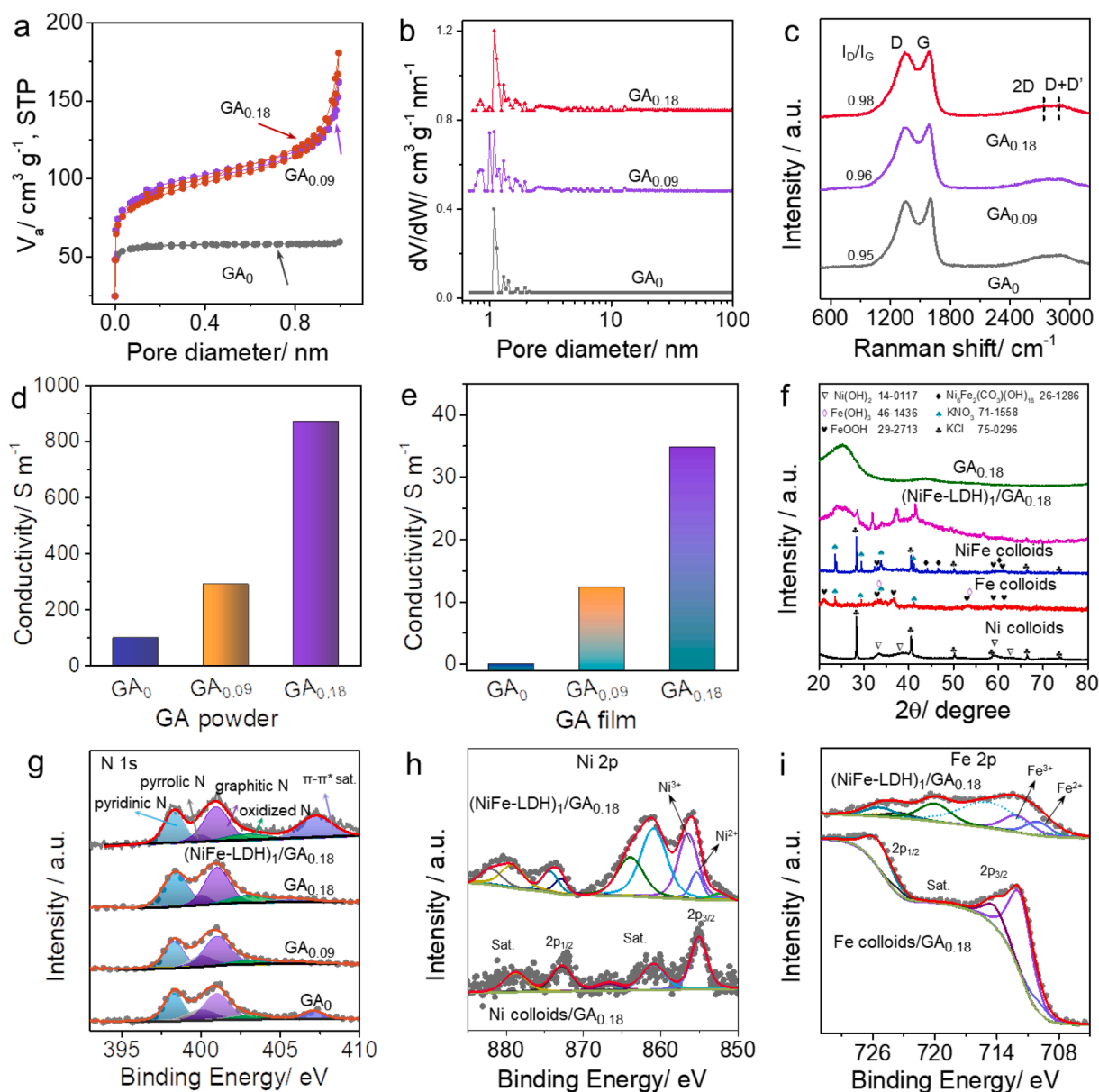
Fig. 2. (a) N_2 adsorption/desorption isotherms, (b) pore size distributions, and (c) Raman spectra of the GA_x samples. Electrical conductivity of the GA_x samples measured with a standard four-probe method at 30 MPa in the (d) absence and (e) presence of a PTFE binder. (f) XRD patterns of the Ni colloids, Fe colloids, NiFe colloids, $(NiFe-LDH)_1/GA_{0.18}$, and $GA_{0.18}$ samples. (g) High-resolution XPS spectra of the N 1 s electrons of the GA_x and $(NiFe-LDH)_1/GA_{0.18}$ samples. High-resolution XPS spectra of the (h) Ni 2p and (i) Fe 2p electrons of Ni colloids, Fe colloids, and $(NiFe-LDH)_1/GA_{0.18}$.

5000 CV cycles. $(NiFe-LDH)_1/GA_{0.18}$ displayed similar stability.

The high performance of $GA_{0.18}$ towards ORR was also manifested in neutral and acidic media. In CV measurements, $GA_{0.18}$ exhibited an E_p of + 0.665 V in 0.1 M phosphate buffer solution (PBS), which was 81 mV more negative than that of Pt/C (+0.746 V) (Fig. 3d). In RDE measurements, the $E_{1/2}$ of $GA_{0.18}$ (+0.701 V) was more positive than those of other GA_x samples and only slightly more negative than that of Pt/C (+0.731 V). For $(NiFe-LDH)_1/GA_{0.18}$, the $E_{1/2}$ was ca. + 0.738 V, again, suggesting that $GA_{0.18}$ and $(NiFe-LDH)_1/GA_{0.18}$ are competitive as compared to the majority of relevant catalysts reported to date in the literature (Fig. 3f and Table S5). In addition, $GA_{0.18}$ exhibited a Tafel slope of 77 mV dec^{-1}, lower than that (93 mV dec^{-1}) of Pt/C (Fig. S7d), with an average electron transfer number (n) 3.89 for $GA_{0.18}$ and 3.93 for Pt/C (Fig. S7e); and the $E_{1/2}$ shifted negatively by only 9 mV after 5000 cycles, demonstrating robust stability, with $(NiFe-LDH)_1/GA_{0.18}$ demonstrating a similar performance (Fig. S7f). Nevertheless, the ORR activity in acidic media of the carbon aerogel composites was obviously subpar as compared to that of Pt/C (Fig. S8).

Remarkably, the $(NiFe-LDH)_nGA_{0.18}$ nanocomposites also exhibited an excellent activity towards OER (Fig. 4a and S9a). As the mass loading of the NiFe-LDH colloids increased in the $(NiFe-LDH)_n/GA_{0.18}$ composites, the overpotential ($\eta_{OER,10}$) needed to reach the current density of 10 mA cm^{-2} decreased markedly, from over + 470 mV for $GA_{0.18}$ to + 282 mV for $(NiFe-LDH)_3/GA_{0.18}$ (NiFe-LDH 0.2 wt%), +226 mV for $(NiFe-LDH)_2/GA_{0.18}$ (NiFe-LDH 1.7 wt%), and only + 223 mV for $(NiFe-LDH)_1/GA_{0.18}$ (NiFe-LDH 14.5 wt%), in comparison to + 358 mV of the NiFe-LDH colloids alone. This suggests that the OER intrinsic activity arose primarily from the NiFe-LDH and was facilitated by the synergistic interactions between NiFe-LDH and the GA scaffold, with minimal contributions from the GA alone, and $(NiFe-LDH)_1/GA_{0.18}$ represents the optimal structure.

Interestingly, $(NiFe-LDH)_1/GA_{0.18}$ displayed a similarly low $\eta_{OER,10}$ of + 213 mV when supported on a nickel foam (NF) and 223 mV with a gas diffusion layer (GDL) (Fig. S9b). To reach a larger current density of
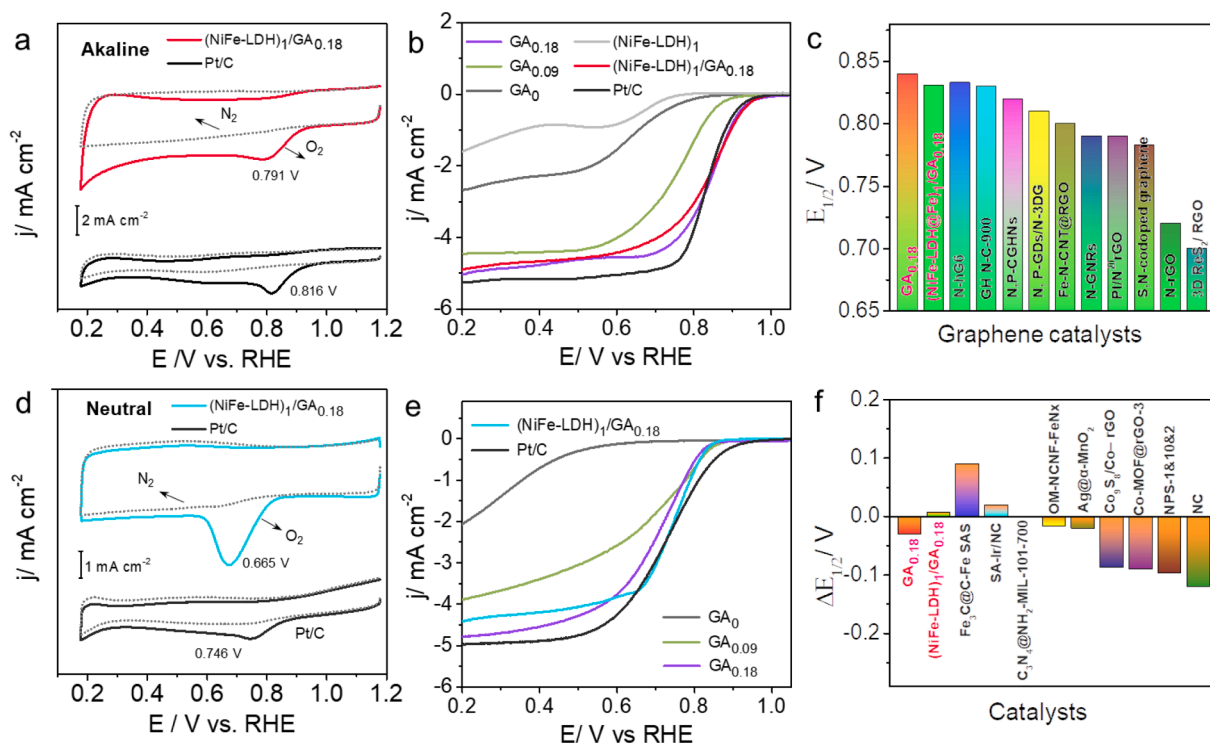
Fig. 3. (a) CV curves of $GA_{0.18}$ and commercial 20 wt% Pt/C in O_2/N_2-saturated 0.1 M KOH at a scan rate of 50 mV s^{-1}. (b) ORR polarization curves at 1600 rpm in O_2-saturated 0.1 M KOH at a scan rate of 5 mV s^{-1}. (c) Comparison of $E_{1/2}$ of $GA_{0.18}$ with graphene-based catalysts reported recently in alkaline media (**Table S4**). (d) CV curves in O_2/N_2-saturated 0.1 M PBS. (e) ORR polarization curves at 1600 rpm in O_2-saturated 0.1 M PBS. (f) Comparison of $\Delta E_{1/2}$ (the difference between the half-wave potentials of nanocomposite samples and 20 wt% Pt/C benchmark) for $GA_{0.18}$ with relevant catalysts reported recently in neutral media (**Table S5**).
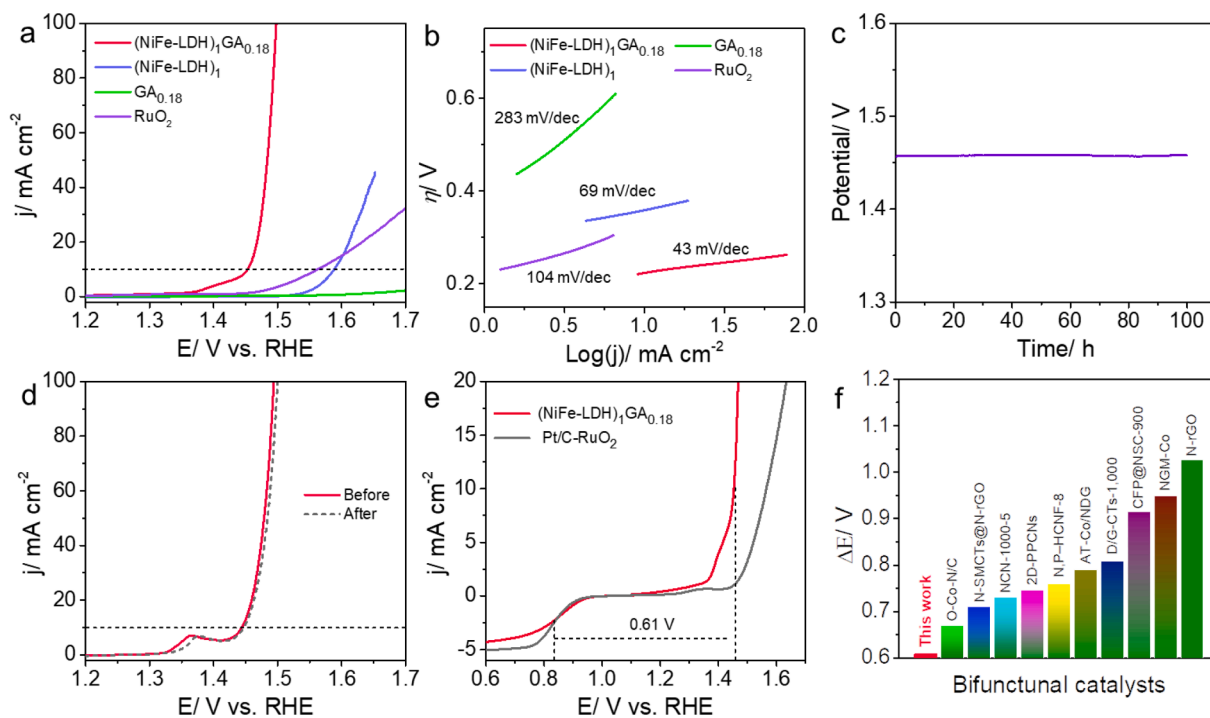
Fig. 4. (a) OER polarization curves in 1 M KOH with the catalysts supported on a gas diffusion layer (GDL), and the corresponding (b) Tafel plots. (c) Chronopotentiometric (CP) profile of $(NiFe-LDH)_1/GA_{0.18}$ supported on NF at the current density of 10 mA cm^{-2} for 100 h. (d) OER polarization curves of $(NiFe-LDH)_1/GA_{0.18}$ supported on NF before and after the CP test. (e) Combined ORR and OER polarization curves, with the OER polarization curves collected with the catalysts supported on a GDL. (f) Comparison of ΔE of $(NiFe-LDH)_1/GA_{0.18}$ and other noble metal-free bifunctional catalysts reported recently (**Table S6**). Note that the ORR and OER performances are tested in 0.1 M KOH and 1 M KOH, respectively.
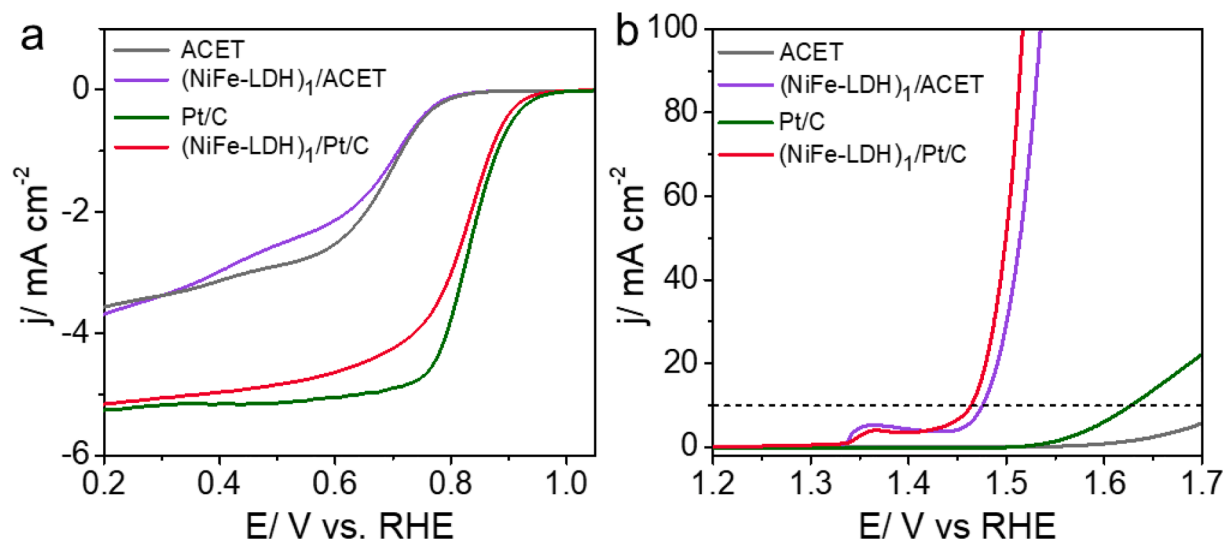
Fig. 5. LSV curves of commercial substrates before and after the adsorption of NiFe colloids for (a) ORR and (b) OER in alkaline media.

50 (100) mA cm^{-2}, the corresponding overpotential was only +246 (+258) mV. Notably, the (NiFe-LDH)$_1$/GA$_{0.18}$ sample even outperformed commercial RuO$_2$ ($\eta_{OER,10}$ = +333 mV) on GDL (Fig. 4a), and a number of noble metal-free catalysts [42]. In addition, (NiFe-LDH)$_1$/GA$_{0.18}$ showed a Tafel slope of 43 mV dec^{-1}, which is the lowest among the sample series, suggesting its fastest electron-transfer kinetics (Fig. 4b **and S10a**). This is consistent with the results from electrochemical impedance measurements (**Fig. S10b-c**), where the charge-transfer resistance (R$_{ct}$) was estimated to be 17 Ω for (NiFe-LDH)$_1$/GA$_{0.18}$, as compared to 20 Ω for (NiFe-LDH)$_2$/GA$_{0.18}$, 348 Ω for (NiFe-LDH)$_3$/GA$_{0.18}$, 3300 Ω for GA$_{0.18}$, and 210 Ω for commercial RuO$_2$.

The stability was evaluated by measuring the OER polarization curves before and after chronopotentiometry (CP) tests for up to 100 h at 10 mA cm^{-2} (Fig. 4c-d), where the $\eta_{OER,10}$ remained virtually unchanged. Finally, the (NiFe-LDH)$_1$GA$_{0.18}$ displayed the highest performance with a potential difference (ΔE) between the E$_{1/2}$ of ORR and E$_{OER,10}$ of OER of only 0.611 V among the noble metal-free bifunctional oxygen catalysts reported recently in the literature (Fig. 4e-f).

To further demonstrate the excellent activity of (NiFe-LDH)$_1$/GA$_{0.18}$ for OER, (NiFe-LDH)$_1$/GA$_{0.18}$ and commercial Pt/C were paired to construct an overall water splitting system. As displayed in **Fig. S11a**, the (NiFe-LDH)$_1$/GA$_{0.18}$//Pt/C cell required a low voltage of only 1.508 V (with a corresponding energy efficiency of 81.6 %) to reach the current density of 10 mA cm^{-2}, as compared to 1.593 V for RuO$_2$//Pt/C (energy efficiency 77.2 %), and outperformed a number of water electrolyzers based on, for instance, Co$_2$P@Co$_3$O$_4$ (1.57 V) [62], NiVB/rGO (1.56 V) [63], and CoP-MNA (1.62 V) [64]. **Fig. S11b** depicts a digital photograph of water splitting with the (NiFe-LDH)$_1$/GA$_{0.18}$//Pt/C cell powered by one AA battery (1.5 V), and the formation of H$_2$ and O$_2$ bubbles can be clearly seen on the cathode and anode surfaces (**Video S1**). Moreover, this cell could work continuously for over 20 h, and the cell voltage remained largely unchanged at the current density of 10 mA cm^{-2}, suggesting remarkable stability and high potential of the (NiFe-LDH)$_1$/GA$_{0.18}$ in overall water splitting (**Fig. S11c-d**).

The NiFe-LDH colloids could also be readily hybridized with other commerical substrates as excellent bifunctional oxygen catalysts, such as carbon nanoparticles of acetylene black (ACET) or commercial 20 wt% Pt/C (**Fig. S12-S13**). Fig. 5a **and 5b** shows the ORR/OER polarization curves of ACET and Pt/C before and after the adsorption of the NiFe-LDH colloids. One can see that the ORR performance remained almost unchanged for both ACET and Pt/C, whereas for OER, the $\eta_{OER,10}$ (+233 mV) for (NiFe-LDH)$_1$/Pt/C became much lower than that of Pt/C (+356 mV), and (NiFe-LDH)$_1$/ACET (+246 mV) was also significantly more active than ACET alone (over + 470 mV). That is, the adsorption of the

bimetal colloids did not impact the ORR activity of the samples, demonstrating the universality of the hybridization method to transform ORR catalysts into excellent bifunctional oxygen catalysts.

2.3. Mechanism insights for OER

Results presented above in section 2.2 demonstrate that the ORR activity arose primarily from the nitrogen dopants in the GA, with essentially no contribution from the NiFe-LDH [23,65]. Yet, the OER activity was most likely ascribed to the NiFe-LDH facilitated by the synergistic interaction between the NiFe-LDH colloid and the GA scaffold. It is therefore important to unravel the mechanistic insights.

It has been argued that the OER activity of NiFe-LDH is mainly due to the high valence-state Ni^{3+}/Ni^{4+} species [66]. This is indeed confirmed in operando Raman measurements at various applied potentials [8,67]. Fig. 6 depicts the Raman spectra of (a) Ni(OH)$_2$ and (b) NiFe-LDH collected with the electrode potential varied from open circuit potential (OCP) to +1.5 V. At potentials below +1.3 V, two characteristic vibrational bands can be identified with Ni(OH)$_2$ at 458 and 539 cm^{-1}, due to the Ni^{II}-OH and Ni^{II}-O vibrations, respectively [68]. At +1.3 V, two new peaks emerged at 476 and 554 cm^{-1}, arising from the Ni^{III}-O vibrations of NiOOH, suggesting the oxidation of Ni^{2+} into Ni^{3+} and Ni^{4+} (Fig. 6a) [68–70]. In comparison, the prominent Ni^{III}-O peaks can be observed even at OCP for NiFe-LDH and became markedly intensified with increasing electrode potential, but was absent for NiFe-LDH without the surface-adsorbed Fe(OH)$_3$ colloids (**Fig. S14**), suggesting that the oxidation of Ni^{2+} to higher valence state was driven by the Fe(OH)$_3$ colloids (Fig. 6b). Note that there were two Fe species in (NiFe-LDH)$_1$/GA$_{0.18}$, the internal lattice Fe in NiFe-LDH and the surface Fe in amorphous Fe(OH)$_3$ nanoparticles adsorbed on the NiFe-LDH surface. The former likely inhibited the oxidation of Ni [66,71], whereas the latter might facilitate the oxidation of Ni at OCP, because of the unsaturated coordination of high valence Fe$^{(3+\delta)+}$ arising from the nano size [72] and amorphous phase of the Fe(OH)$_3$ colloids [73].

The charge density difference indeed revealed the influence of amorphous Fe(OH)$_3$ nanoparticles on the electronic structure of NiFe-LDH (Fig. 7a). The Fe:Ni atomic ratio of the NiFe-LDH model is ca. 7:2, which is the optimum ratio of NiFe-LDH for OER [74]. In comparison to pristine NiFe-LDH, the surface Fe(OH)$_3$ colloids led to a more delocalized charge density of NiFe-LDH, especially at the Ni centers, which facilitated the generation of high valence states of the Ni sites [75,76]. Such different characteristics in charge configuration are in good agreement with the results of the above operando Raman measurements.

DFT calculations were then conducted to evaluate the Gibbs free energy of the formation of key reaction intermediates (i.e., OH*, O* and OOH*) along the elementary pathway, according to the conventional four-electron transfer and the lattice oxygen mechanism on NiFe-LDH with and without surface Fe(OH)$_3$ colloids [77,78]. The calculation results show that the formation of these intermediates on pristine Ni-LDH is negligible, and entailed a higher energy barrier than that on Fe(OH)$_3$ modified NiFe-LDH [66,79]. **Fig. S15-S16** display the optimized structure of pristine NiFe-LDH and Fe(OH)$_3$ modified NiFe-LDH with the adsorption of different intermediates onto the bridging oxygen between the Fe and Ni atoms adjacent to the Fe(OH)$_3$ nanoparticles. The corresponding free energy diagrams are shown in Fig. 7**b-c**. The largest free energy difference occurred at the formation of O* for pristine FeNi-LDH with an energy barrier of 0.87 eV at U = 1.23 V, suggesting that this was the rate determining step (RDS) [66,77]. Note that the energy barrier of this same step was significantly reduced to −0.31 eV for the Fe(OH)$_3$ modified FeNi-LDH, likely due to enhanced adsorption of oxygen on the Ni sites, where electrons were more delocalized, and the formation of OH* now became the RDS, with an energy barrier of only 0.42 eV, leading to enhanced OER catalysis. The theoretical trend is very consistent with the experimental results [42] and the positive relationship between the Fe(OH)$_3$ coverage and OER activity of NiFe-LDH [32].

The local density of states (LDOS) at the Fe and Ni sites are depicted in **Fig. S17**. In comparison with pristine NiFe-LDH, the d-band of the Fe sites became lower while that of the Ni sites shifted positively for the Fe(OH)$_3$ modified FeNi-LDH. It is well-konwn that a higher d-band center facilates a greater binding energy of oxygen intermediates, such as OH*. That is, the adsorption of Fe(OH)$_3$ colloids onto the NiFe-LDH surface may optimize the binding of OH*, leading to an enhanced OER activity [80].

2.4. Applications in alkaline/neutral zinc-air batteries

Because of the excellent bifunctional ORR and OER activity, the practical application of (NiFe-LDH)$_1$/GA$_{0.18}$ was further assessed as the oxygen catalysts in rechargeable ZAB, in comparison with the Pt/C-RuO$_2$ commercial benchmarks. From **Fig. 8a**, the (NiFe-LDH)$_1$/GA$_{0.18}$ based ZAB can be seen to exhibit an OCP of 1.505 V, which is much higher than that (1.453 V) based on the Pt/C-RuO$_2$ mixture. The peak power density of 230 mW cm^{-2} for the former is also nearly twice that (146 mW cm^{-2}) of the latter, likely due to the abundant oxygen supply enabled by the 3D porous structure and the ultrahigh electrical conductivity of the graphene aerogel (**Fig. 8b**). Consequently, the (NiFe-

LDH)$_1$/GA$_{0.18}$ based ZAB showed an enhanced specific capacity of 749 mAh g$_{zn}^{-1}$ and energy density of 951 mWh g$_{zn}^{-1}$, as compared to 725 mAh g$_{zn}^{-1}$ and 908 mWh g$_{zn}^{-1}$ for the Pt/C-RuO$_2$ counterpart (**Fig. 8c**). The (NiFe-LDH)$_1$/GA$_{0.18}$ based ZAB also displayed higher discharge voltages at various current densities (**Fig. 8d**), for instance, 1.17 V at 50 mA cm^{-2} and 1.08 V at 100 mA cm^{-2}, as compared to 0.993 V and 0.731 V for the Pt/C-RuO$_2$ ZAB.

(NiFe-LDH)$_1$/GA$_{0.18}$ could also work for a rechargeable ZAB for an extended period of time, and exhibited virtually no decay for over 340 h in both short-period cycling and consecutive long-period cycling tests, in contrast to Pt/C-RuO$_2$ (**Fig. 8e-f and S18a**). The voltage gap between charge and discharge is also practically unchanged, except for the initial stage, suggesting optimization of the active sites for (NiFe-LDH)$_1$/GA$_{0.18}$. For the long-period cycling (2 h per cycle), the (NiFe-LDH)$_1$/GA$_{0.18}$ based ZAB could continuously operate for over 100 h, featuring stable charge and discharge voltage platforms for up to 53 cycles (**Fig. S18b**), with only a negligible change of the energy efficiency from 60.2 % in the 1st cycle to 58.3 % in the 53rd (**Fig. 8f**). Note that the cycling period has an important influence on the energy efficiency of ZABs (**Table S8**). Yet during the long-period cycling tests, the energy efficiency remained higher (60 % at 10 mAh cm^{-2}) than other reported ZABs (42 ~ 61 % at 0.5 ~ 2 mAh cm^{-2}), and almost met the basic requirement to compete with Li-ion cells [2,5], suggesting high potential in practical applications.

The application of (NiFe-LDH)$_1$/GA$_{0.18}$ in flexible alkaline solid-state rechargeable ZAB was also assessed, in comparison to Pt/C-RuO$_2$. The (NiFe-LDH)$_1$/GA$_{0.18}$ based solid battery showed an OCP of ca. 1.32 V with a maximum power density of 166 mW cm^{-2}, much higher than that for the Pt/C-RuO$_2$ counterpart (1.27 V and 86 mW cm^{-2}) (**Fig. 9a**). In addition, the OCP of the (NiFe-LDH)$_1$/GA$_{0.18}$ battery remained stable when the device was bent from 0° to 90° and 180° (**Fig. 9b**), and could successfully power an electronic clock (**Video S2**) and lit up a LED (light-emitting diode) (**Fig. 9c and S19a**), suggesting good mechanical flexibility. Furthermore, the charge and discharge performance of the (NiFe-LDH)$_1$/GA$_{0.18}$ solid battery remained virtually unchanged for over 85 h, even in long-period cycling, suggesting robust stability (**Fig. 9d-e, and S19b-c**). A similarly remarkable performance was also observed in neutral media (**Fig. S20, Video S3, and Table S9**).

Microscopic and spectroscopic measurements showed that the (NiFe-LDH)$_1$/GA$_{0.18}$ catalysts remained structurally stable after the cycling charge and discharge tests in the rechargeable ZABs (**Fig. S21-S22**). From the high angle annular dark-field scanning transmission electron microscopy (HAADF-STEM) image in **Fig. S22a**, it can be seen that the
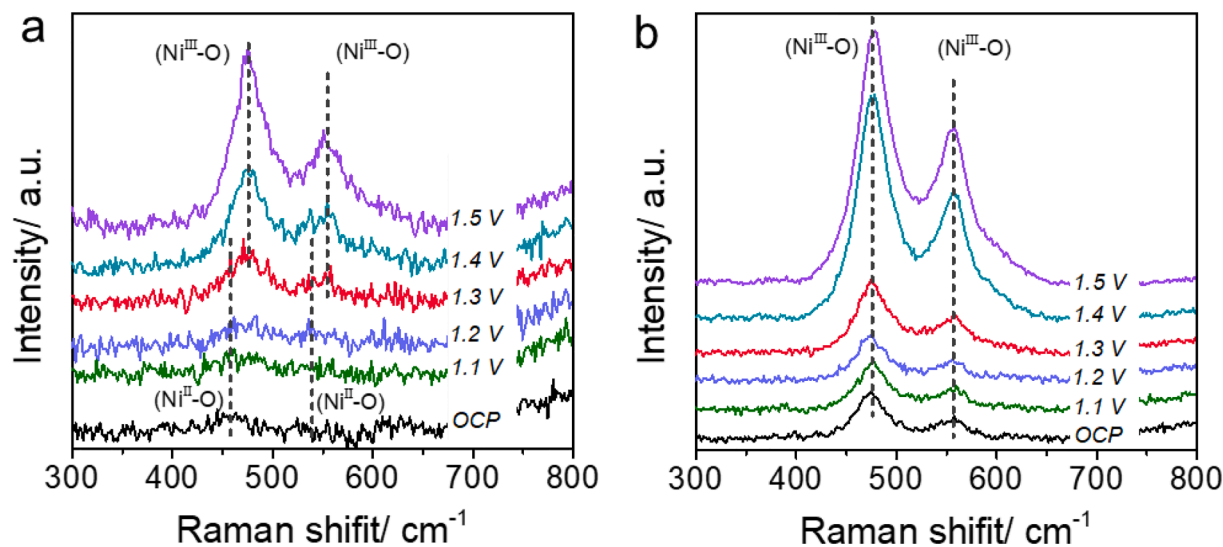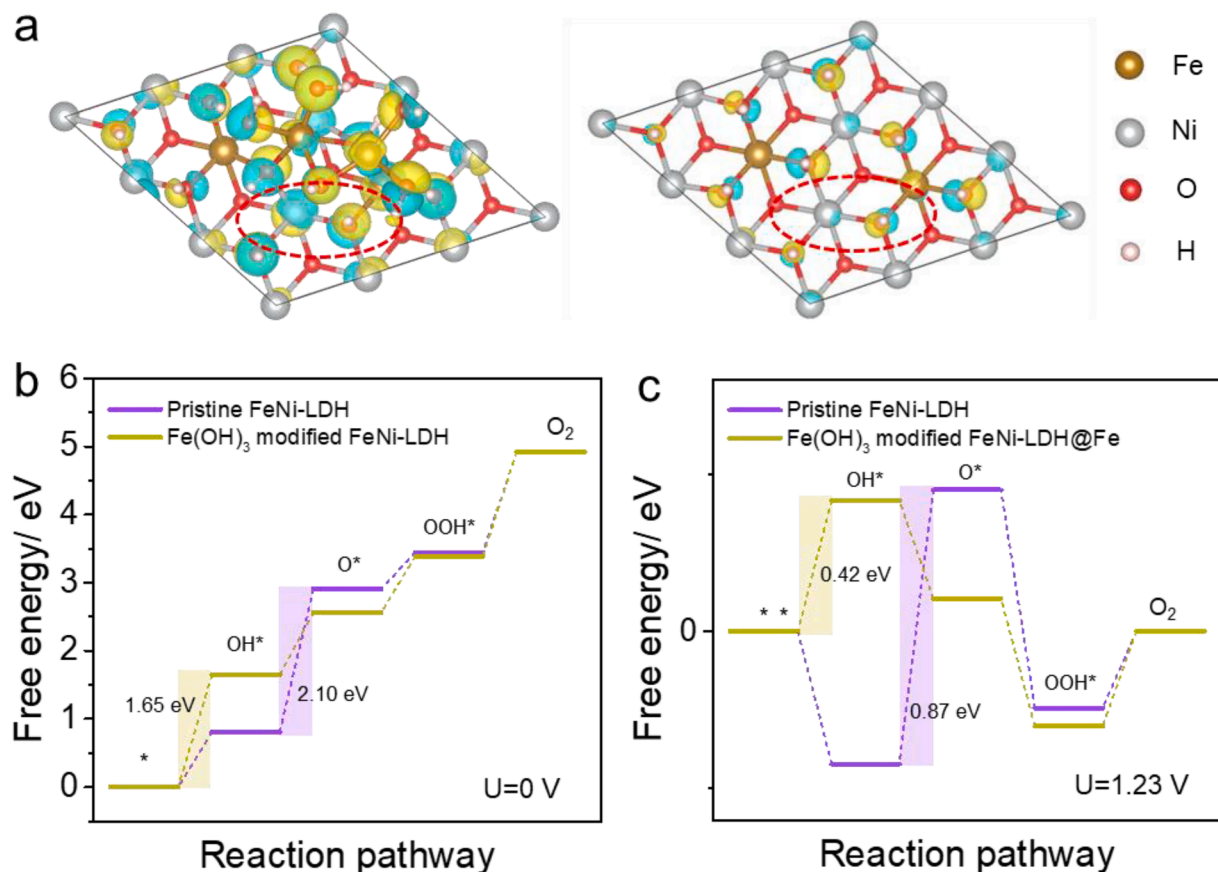

Fig. 6. Operando Raman spectra of the Ni-O vibrations in (a) Ni(OH)$_2$ and (b) NiFe-LDH at different applied potentials.

Fig. 7. (a) Charge density difference of Fe(OH)$_3$ modified FeNi-LDH (left) and pristine NiFe-LDH (right). Yellow and blue regions represent charge accumulation and depletion, respectively. The Ni atom in the red cycles is the actve site for OER. Free energy diagrams of OER on Fe(OH)$_3$ modified FeNi-LDH and pristine NiFe-LDH at (b) U = 0 V and (c) 1.23 V.
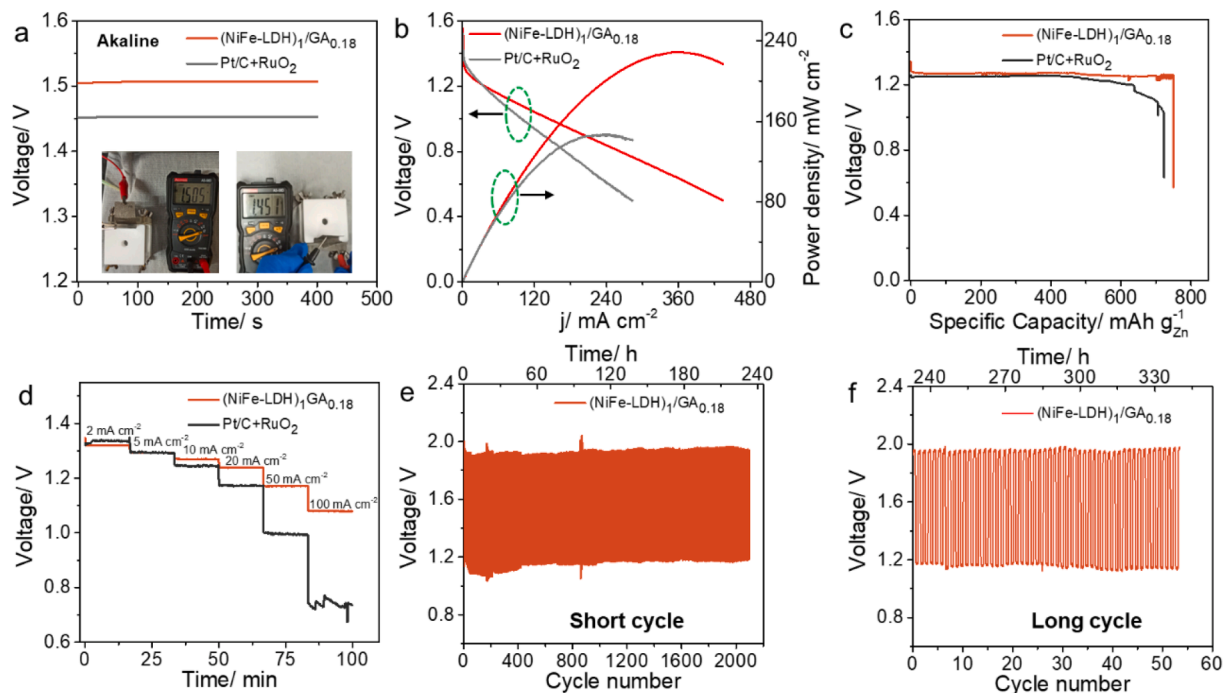
Fig. 8. (a) Open-circuit potential (OCP, insets are the photographs of the measurements), (b) discharge polarization and power density curves, (c) galvanostatic discharge and specific capacity curves, and (d) galvanostatic discharge curves at various current densities of (NiFe-LDH)$_1$/GA$_{0.18}$ and Pt/C-RuO$_2$ based ZABs. (e) Short cycle time charge–discharge curves (2100 cycles) and (f) Long cycle time charge–discharge curves (53 cycles) of the (NiFe-LDH)$_1$/GA$_{0.18}$ based ZAB at 10 mA cm^{-2} for ca. 340 h.
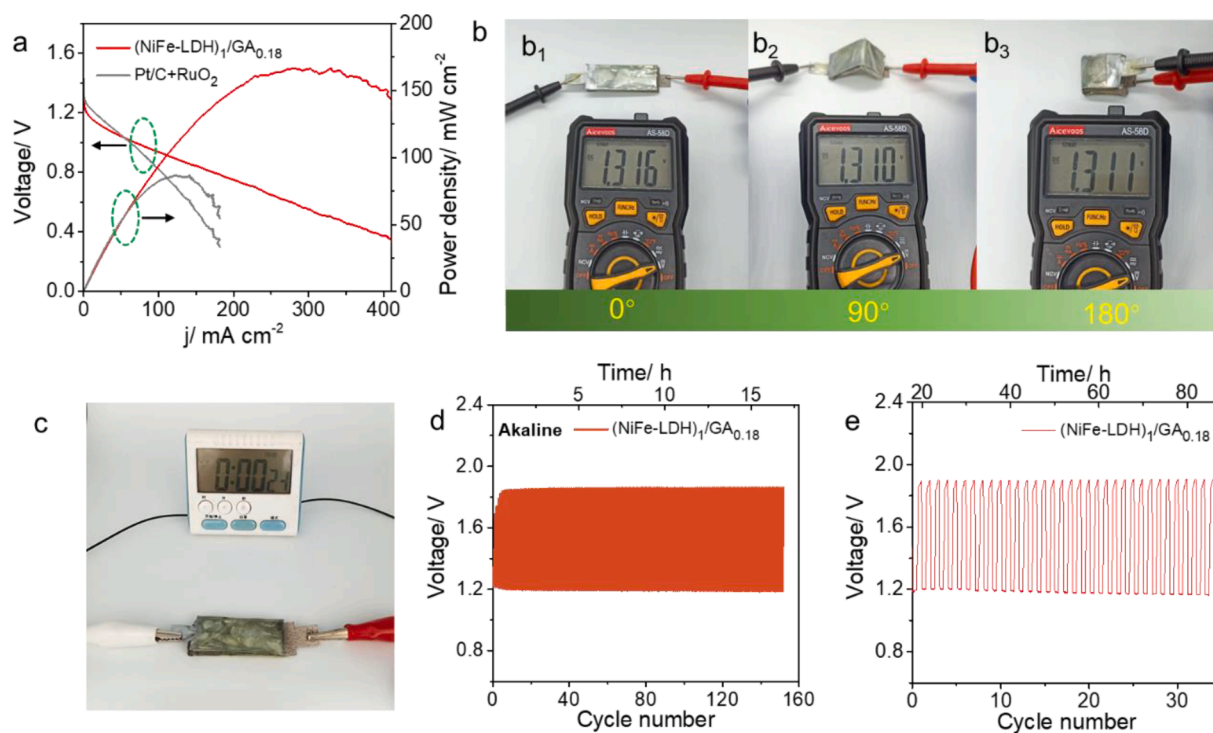
Fig. 9. (a) Discharge polarization and power density curves of $(NiFe\text{-}LDH)_1/GA_{0.18}$ and $Pt/C\text{-}RuO_2$-based Zn–air batteries. (b) Photographs of Zn–air battery based on $(NiFe\text{-}LDH)_1/GA_{0.18}$ with OCPs measured with the battery before bending (0°) and after being bent to 90° and 180°. (c) Photos of an electronic clock powered by a $(NiFe\text{-}LDH)_1/GA_{0.18}$ based solid Zn–air battery. (d) Short-period charge–discharge curves (400 s per cycle for 150 cycles) and (e) long-period charge–discharge curves (2 h per cycle for 34 cycles) of the $(NiFe\text{-}LDH)_1/GA_{0.18}$ based solid Zn-air battery at 5 mA cm^{-2}.

NiFe-LDH colloidal particles remained well-dispersed on the GA surface, and the EDS mapping analysis exhibited almost no variation of the distributions of the Ni and Fe elements before and after the stability tests. Additionally, inductively coupled plasma-mass spectrometry (ICP-MS) measurements showed that the sample retained 94.8% Ni and 97.4% Fe of the original contents, further confirming the good stability of the NiFe-LDH colloids. Yet, XPS studies showed an increase of oxygen vacancies (Vo) (from 0 to 1.0 at%, **Table S3, Fig. S22b**) and enhanced electron-deficient Ni sites, which might account for the optimization of the cycling performance for ZAB. From **Fig. S22c**, it can be seen that the nitrogen species disappeared completely except for the pyridine group, indicating the stability of pyridine N and unstable role of graphitic N [53]; and Vo, a type of active sites for ORR and OER [81], was generated during the battery test (**Fig. S22b**), likely because lattice oxygen of metal oxides was oxidized into O_2 during the OER process [82]. In addition, oxygen vacancies may also result from metal reduction in aerobic environment [83,84]. Interestingly, as compared to the Ni $2p_{3/2}$ binding energy before the cycling test (**Fig. S22d**), the corresponding peak position of $(NiFe\text{-}LDH)_1/GA_{0.18}$ shifted positively and the Ni^{2+}/Ni ratio decreased from 20% to 7%; meanwhile, the $Fe^{3+}/(Fe^{3+}+Fe^{2+})$ ratio decreased from 59% of the original sample to 22% after cycling test (**Fig. S22e**), suggesting enhanced electron transfer from Ni^{2+} to Fe^{3+} and the activation of nickel active sites.

3. Conclusion

In summary, ultrathin carbon aerogels with few-layer graphene in the skeletons were readily prepared by controlled pyrolysis of a hydrogel precursor using arrays of cubic NaCl crystals as the removable template. Despite the thin carbon skeletons, the aerogels exhibited high electrical conductivity and low mass density, along with good porosity. Such a unique structure rendered the $GA_{0.18}$ the best catalyst for ORR. Meanwhile, the OER performance of NiFe-LDH was enhanced by the surface-adsorbed $Fe(OH)_3$ colloids, due to the modulation of the binding energy

of key reaction intermediates and reduction of the energy barrier. This is further facilitated by the synergisic interaction between the NiFe-LDH colloids and the GA scaffold. Therefore, the deposition of NiFe nano-colloids onto the GA matrix rendered the composites bifunctionally active towards both ORR and OER. The best sample, $(NiFe\text{-}LDH)_1/GA_{0.18}$ showed a ΔE of only 0.61 V, that was markedly lower than those of the $Pt/C\text{-}RuO_2$ commercial benchmarks and relevant catalysts in the literature. When the $(NiFe\text{-}LDH)_1/GA_{0.18}$ was coupled with Pt/C, effective water-splitting was observed with an energy efficiency of 81.7% at the current density of 10 mA cm^{-2}. In addition, $(NiFe\text{-}LDH)_1/GA_{0.18}$ could be used as effective oxygen electrocatalysts in rechargeable ZABs, featuring a power density of 230 and 112 mW cm^{-2} in alkaline and neutral media, respectively, about twice that with commercial $Pt/C\text{-}RuO_2$. The former also displayed a high energy efficiency of 60.2 % over 340 h at 10 mAh cm^{-2}, rather competitive to Li-ion batteries. Results from this work demonstrate the unique potential of ultrathin carbon aerogels in the development of high-performance, low-cost catalysts for electrochemical energy technologies.

CRediT authorship contribution statement

Qiang Li: Data curation, Formal analysis, Writing – original draft. **Zhifang Sun:** Data curation, Formal analysis. **Chunyang Yin:** Data curation, Formal analysis. **Yang Chen:** Data curation, Formal analysis. **Dingjie Pan:** Formal analysis, Writing – review & editing. **Bingzhe Yu:** Formal analysis, Writing – review & editing. **Yi Zhang:** Conceptualization, Funding acquisition, Project administration, Writing – original draft. **Ting He:** Formal analysis, Writing – original draft. **Shaowei Chen:** Formal analysis, Funding acquisition, Writing – review & editing.

Declaration of Competing Interest

The authors declare that they have no known competing financial interests or personal relationships that could have appeared to influence

the work reported in this paper.

Data availability

Data will be made available on request.

Acknowledgements

Appendix A. Supplementary data

Supplementary data to this article can be found online at https://doi.org/10.1016/j.cej.2023.141492.

References

[1] R. Chen, X. Xu, S. Peng, J. Chen, D. Yu, C. Xiao, Y. Li, Y. Chen, X. Hu, M. Liu, H. Yang, I. Wyman, X. Wu, A Flexible and Safe Aqueous Zinc-Air Battery with a Wide Operating Temperature Range from-20 to 70 degrees C, ACS Sustain. Chem. Eng. 8 (2020) 11501–11511.

[2] Y. Li, J. Lu, Metal-air batteries: will they be the future electrochemical energy storage device of choice? ACS Energy Lett. 2 (2017) 1370–1377.

[3] Y. Xue, Y. Guo, Q. Zhang, Z. Xie, J. Wei, Z. Zhou, MOF-Derived Co and Fe Species Loaded on N-Doped Carbon Networks as Efficient Oxygen Electrocatalysts for Zn-Air Batteries, Nano-Micro Lett 14 (2022) 162.

[4] L. Xu, S. Wu, X. He, H. Wang, D. Deng, J. Wu, H. Li, Interface Engineering of Anti-Perovskite Ni3FeN/VN Heterostructure for High-Performance Rechargeable Zinc-Air batteries, Chem. Eng. J. 437 (2022), 135291.

[5] J.F. Parker, J.S. Ko, D.R. Rolison, J.W. Long, Translating Materials-Level Performance into Device-Relevant Metrics for Zinc-Based Batteries, Joule 2 (2018) 2519–2527.

[6] Y. Guo, S. Yao, L. Gao, A. Chen, M. Jiao, H. Cui, Z. Zhou, Boosting bifunctional electrocatalytic activity in S and N co-doped carbon nanosheets for high-efficiency Zn–air batteries, J. Mater. Chem. A 8 (2020) 4386–4395.

[7] L. Wang, L. Zhang, W. Ma, H. Wan, X. Zhang, X. Zhang, S. Jiang, J.Y. Zheng, Z. Zhou, In Situ Anchoring Massive Isolated Pt Atoms at Cationic Vacancies of α-NixFe1-x(OH)2 to Regulate the Electronic Structure for Overall Water Splitting, Adv. Funct. Mater. 32 (2022) 2203342.

[8] J. Ge, J.Y. Zheng, J. Zhang, S. Jiang, L. Zhang, H. Wan, L. Wang, W. Ma, Z. Zhou, R. Ma, Controllable atomic defect engineering in layered NixFe1−x(OH)2 nanosheets for electrochemical overall water splitting, J. Mater. Chem. A 9 (2021) 14432–14443.

[9] Z. Cai, L. Li, Y. Zhang, Z. Yang, J. Yang, Y. Guo, L. Guo, Amorphous Nanocages of Cu-Ni-Fe Hydr(oxy)oxide Prepared by Photocorrosion For Highly Efficient Oxygen Evolution, Angew. Chem. Int. Ed. 58 (2019) 4189–4194.

[10] N. Xu, J. Qiao, Recent progress in bifunctional catalysts for zinc-air batteries, J Electrochem 26 (2020) 531–562.

[11] Y. Wang, Y. Zhao, L. Liu, W. Qin, S. Liu, J. Tu, Y. Qin, J. Liu, H. Wu, D. Zhang, A. Chu, B. Jia, X. Qu, M. Qin, Mesoporous Single Crystals with Fe-Rich Skin for Ultralow Overpotential in Oxygen Evolution Catalysis, Adv. Mater. 34 (2022) e2200088.

[12] P. Prabhu, J.M. Lee, Metallenes as functional materials in electrocatalysis, Chem. Soc. Rev. 50 (2021) 6700–6719.

[13] H. Wang, J. Li, K. Li, Y. Lin, J. Chen, L. Gao, V. Nicolosi, X. Xiao, J.M. Lee, Transition metal nitrides for electrochemical energy applications, Chem. Soc. Rev. 50 (2021) 1354–1390.

[14] Y. Zhu, S. Murali, M.D. Stoller, K.J. Ganesh, W. Cai, P.J. Ferreira, A. Pirkle, R. M. Wallace, K.A. Cychosz, M. Thommes, D. Su, E.A. Stach, R.S. Ruoff, Carbon-based supercapacitors produced by activation of graphene, Science 332 (2011) 1537–1541.

[15] P.N. Nirmalraj, T. Lutz, S. Kumar, G.S. Duesberg, J.J. Boland, Nanoscale mapping of electrical resistivity and connectivity in graphene strips and networks, Nano Lett. 11 (2011) 16–22.

[16] L. Kong, X. Yin, M. Han, X. Yuan, Z. Hou, F. Ye, L. Zhang, L. Cheng, Z. Xu, J. Huang, Macroscopic bioinspired graphene sponge modified with in-situ grown carbon nanowires and its electromagnetic properties, Carbon 111 (2017) 94–102.

[17] H. Sun, L. Mei, J. Liang, Z. Zhao, C. Lee, H. Fei, M. Ding, J. Lau, M. Li, C. Wang, X. Xu, G. Hao, B. Papandrea, I. Shakir, B. Dunn, Y. Huang, X. Duan, Three-dimensional holey-graphene/niobia composite architectures for ultrahigh-rate energy storage, Science 356 (2017) 599–604.

[18] L. Qiu, J.Z. Liu, S.L. Chang, Y. Wu, D. Li, Biomimetic superelastic graphene-based cellular monoliths, Nat. Commun. 3 (2012) 1241.

[19] X. Zhang, D. Zhang, Z. Xu, K. Zhang, Y. Zhang, M. Jing, L. Liu, Z. Zhang, N. Pu, J. Liu, C. Yan, A pioneering melamine foam-based electrode via facile synthesis as prospective direction for vanadium redox flow batteries, Chem. Eng. J. 439 (2022), 135718.

[20] J.H. Kim, J.M. Kim, G.W. Lee, G.H. Shim, S.T. Lim, K.M. Kim, T.T. Nguyen Vo, B. Kweon, S. Wongwises, D.W. Jerng, M.H. Kim, H.S. Ahn, Advanced Boiling-A Scalable Strategy for Self-Assembled Three-Dimensional Graphene, ACS Nano 15 (2021) 2839–2848.

[21] B. Yaru, W. Hao, H. Jintang, L. Bowen, L. Dong, D. Liming, Nitrogen-rich holey graphene for efficient oxygen reduction reaction, Carbon 162 (2020) 66–73.

[22] L. Dos Santos-Gomez, J.R. Garcia, M.A. Montes-Moran, J.A. Menendez, S. Garcia-Granda, A. Arenillas, Ultralight-Weight Graphene Aerogels with Extremely High Electrical Conductivity, Small 17 (2021) e2103407.

[23] W. Niu, L. Li, X. Liu, N. Wang, J. Liu, W. Zhou, Z. Tang, S. Chen, Mesoporous N-doped carbons prepared with thermally removable nanoparticle templates: an efficient electrocatalyst for oxygen reduction reaction, J. Am. Chem. Soc. 137 (2015) 5555–5562.

[24] X. Qin, S. Zhu, L. Zhang, S. Sun, M. Shao, Theoretical Studies of Metal-N-C for Oxygen Reduction and Hydrogen Evolution Reactions in Acid and Alkaline Solutions, J Electrochem 27 (2021) 185–194.

[25] X. Hu, Y. Chen, M. Zhang, G. Fu, D. Sun, J.-M. Lee, Y. Tang, Alveolate porous carbon aerogels supported Co9S8 derived from a novel hybrid hydrogel for bifunctional oxygen electrocatalysis, Carbon 144 (2019) 557–566.

[26] J. Chen, C. Fan, X. Hu, C. Wang, Z. Huang, G. Fu, J.M. Lee, Y. Tang, Hierarchically Porous Co/Cox My (M = P, N) as an Efficient Mott-Schottky Electrocatalyst for Oxygen Evolution in Rechargeable Zn-Air Batteries, Small 15 (2019) e1901518.

[27] X. Jiang, K. Liu, Q. Li, M. Liu, M. Yang, X. Chen, B-doped Core-Shell Fe@BC Nanozyme: Active Site Identification and Bacterial Inhibition, Chem. Commun. 57 (2021) 1623–1626.

[28] V. Jose, J.M.V. Nsanzimana, H. Hu, J. Choi, X. Wang, J.M. Lee, Highly Efficient Oxygen Reduction Reaction Activity of N-Doped Carbon-Cobalt Boride Heterointerfaces, Adv. Energy Mater. 11 (2021) 2100157.

[29] T. He, Y. Chen, Q. Liu, B. Lu, X. Song, H. Liu, M. Liu, Y.N. Liu, Y. Zhang, X. Ouyang, S. Chen, Theory-Guided Regulation of FeN4 Spin State by Neighboring Cu Atoms for Enhanced Oxygen Reduction Electrocatalysis in Flexible Metal-Air Batteries, Angew. Chem. Int. Ed. 61 (2022) e202201007.

[30] J. Liu, Z. Gong, C. Allen, W. Ge, H. Gong, J. Liao, J. Liu, K. Huang, M. Yan, R. Liu, G. He, J. Dong, G. Ye, H. Fei, Edge-hosted Fe-N3 sites on a multiscale porous carbon framework combining high intrinsic activity with efficient mass transport for oxygen reduction, Chem Catal 1 (2021) 1291–1307.

[31] L. Trotochaud, S.L. Young, J.K. Ranney, S.W. Boettcher, Nickel-Iron Oxyhydroxide Oxygen-Evolution Electrocatalysts: The Role of Intentional and Incidental Iron Incorporation, J. Am. Chem. Soc. 136 (2014) 6744–6753.

[32] D.Y. Chung P.P. Lopes P. Farinazzo Bergamo Dias Martins, H. He, T. Kawaguchi, P. Zapol, H. You, D. Tripkovic, D. Strmcnik, Y. Zhu, S. Seifert, S. Lee, V.R. Stamenkovic, N.M. Markovic, Dynamic stability of active sites in hydr(oxy)oxides for the oxygen evolution reaction, Nat Energy 5 2020 222 230.

[33] J. Shah, Q. Xie, Z. Kuang, R. Ge, W. Zhou, D. Liu, A.I. Rykov, X. Li, J. Luo, J. Wang, In-Situ/Operando57Fe Mössbauer Spectroscopic Technique and Its Applications in NiFe-based Electrocatalysts for Oxygen Evolution Reaction, J Electrochem 28 (2022), 210854.

[34] X. Zhang, Y. Zhao, Y. Zhao, R. Shi, G.I.N. Waterhouse, T. Zhang, A Simple Synthetic Strategy toward Defect-Rich Porous Monolayer NiFe-Layered Double Hydroxide Nanosheets for Efficient Electrocatalytic Water Oxidation, Adv. Energy Mater. 9 (2019) 1900881.

[35] B.Z. Lu, Q.M. Liu, C.Y. Wang, Z. Masood, D.J. Morris, F. Nichols, R. Mercado, P. Zhang, Q.F. Ge, H.L.L. Xin, S.W. Chen, Ultrafast Preparation of Nonequilibrium FeNi Spinels by Magnetic Induction Heating for Unprecedented Oxygen Evolution Electrocatalysis, Research 2022 (2022) 9756983.

[36] X. Xie, L. Shang, R. Shi, G.I.N. Waterhouse, J. Zhao, T. Zhang, Tubular assemblies of N-doped carbon nanotubes loaded with NiFe alloy nanoparticles as efficient bifunctional catalysts for rechargeable zinc-air batteries, Nanoscale 12 (2020) 13129–13136.

[37] G. Fu, X. Yan, Y. Chen, L. Xu, D. Sun, J.M. Lee, Y. Tang, Boosting Bifunctional Oxygen Electrocatalysis with 3D Graphene Aerogel-Supported Ni/MnO Particles, Adv. Mater. 30 (2018) 1704609.

[38] G. Fu, J. Wang, Y. Chen, Y. Liu, Y. Tang, J.B. Goodenough, J.-M. Lee, Exploring Indium-Based Ternary Thiospinel as Conceivable High-Potential Air-Cathode for Rechargeable Zn-Air Batteries, Adv. Energy Mater. 8 (2018) 1802263.

[39] D. Zhou, Z. Cai, X. Lei, W. Tian, Y. Bi, Y. Jia, N. Han, T. Gao, Q. Zhang, Y. Kuang, J. Pan, X. Sun, X. Duan, NiCoFe-Layered Double Hydroxides/N-Doped Graphene Oxide Array Colloid Composite as an Efficient Bifunctional Catalyst for Oxygen Electrocatalytic Reactions, Adv. Energy Mater. 8 (2018) 1701905.

[40] W.H. Niu, L.G. Li, N. Wang, S.B. Zeng, J. Liu, D.K. Zhao, S.W. Chen, Volatilizable template-assisted scalable preparation of honeycomb-like porous carbons for efficient oxygen electroreduction, J. Mater. Chem. A 4 (2016) 10820–10827.

[41] W.H. Niu, L.G. Li, S.W. Chen, Recent Progress in Template-Assisted Synthesis of Nitrogen-Doped Porous Carbons for Oxygen Electroreduction, J Electrochem 23 (2017) 110–122.

[42] Q. Li, T. He, X. Jiang, Y. Lei, Q. Liu, C. Liu, Z. Sun, S. Chen, Y. Zhang, Boosting oxygen evolution activity of nickel iron hydroxide by iron hydroxide colloidal particles, J Colloid Interf Sci 606 (2022) 518–525.

[43] Z. Wang, L. Xu, F. Huang, L. Qu, J. Li, K.A. Owusu, Z. Liu, Z. Lin, B. Xiang, X. Liu, K. Zhao, X. Liao, W. Yang, Y.B. Cheng, L. Mai, Copper-Nickel Nitride Nanosheets as Efficient Bifunctional Catalysts for Hydrazine-Assisted Electrolytic Hydrogen Production, Adv. Energy Mater. 9 (2019) 1900390.

[44] D. Guan, W. Zhou, Z. Shao, Rational Design of Superior Electrocatalysts for Water Oxidation: Crystalline or Amorphous Structure? Small Sci 1 (2021) 2100030.

[45] L. Zhou, L. Fox, M. Włodek, L. Islas, A. Slastanova, E. Robles, O. Bikondoa, R. Harniman, N. Fox, M. Cattelan, W.H. Briscoe, Surface structure of few layer graphene, Carbon 136 (2018) 255–261.

[46] J. Albero, A. Vidal, A. Migani, P. Concepcion, L. Blancafort, H. Garcia, Phosphorus-Doped Graphene as a Metal-Free Material for Thermochemical Water Reforming at Unusually Mild Conditions, ACS Sustain. Chem. Eng. 7 (2019) 838–846.

[47] A.R. Soleymani, S.M. Rafigh, M. Hekmati, Green synthesis of RGO/Ag: As evidence for the production of uniform mono-dispersed nanospheres using microfluidization, Appl. Surf. Sci. 518 (2020), 146264.

[48] L.G. Cancado, A. Jorio, E.H. Ferreira, F. Stavale, C.A. Achete, R.B. Capaz, M. V. Moutinho, A. Lombardo, T.S. Kulmala, A.C. Ferrari, Quantifying defects in graphene via Raman spectroscopy at different excitation energies, Nano Lett. 11 (2011) 3190–3196.

[49] X. Chen, D. Lai, B. Yuan, M.-L. Fu, Fabrication of superelastic and highly conductive graphene aerogels by precisely "unlocking" the oxygenated groups on graphene oxide sheets, Carbon 162 (2020) 552–561.

[50] D. Deng, J. Qian, X. Liu, H. Li, D. Su, H. Li, H. Li, L. Xu, Non-Covalent Interaction of Atomically Dispersed Cu and Zn Pair Sites for Efficient Oxygen Reduction Reaction, Adv. Funct. Mater. 32 (2022) 2203471.

[51] C.F. Holder, R.E. Schaak, Tutorial on Powder X-ray Diffraction for Characterizing Nanoscale Materials, ACS Nano 13 (2019) 7359–7365.

[52] S. Wu, D. Deng, E. Zhang, H. Li, L. Xu, CoN nanoparticles anchored on ultra-thin N-doped graphene as the oxygen reduction electrocatalyst for highly stable zinc-air batteries, Carbon 196 (2022) 347–353.

[53] Q. Li, T. He, Y.Q. Zhang, H.Q. Wu, J.J. Liu, Y.J. Qi, Y.P. Lei, H. Chen, Z.F. Sun, C. Peng, L.Z. Yi, Y. Zhang, Biomass Waste-Derived 3D Metal-Free Porous Carbon as a Bifunctional Electrocatalyst for Rechargeable Zinc-Air Batteries, ACS Sustain. Chem. Eng. 7 (2019) 17039–17046.

[54] R. Shalvoy, Characterization of coprecipitated nickel on silica methanation catalysts by X-ray photoelectron spectroscopy, J. Catal. 56 (1979) 336–348.

[55] L. Zhang, H. Chuai, H. Liu, q. Fan, S. Kuang, S.S. Zhang, X. Ma, Facet Dependent Oxygen Evolution Activity of Spinel Cobalt Oxides, J Electrochem, 28 (2022) 2108481.

[56] N.S. McIntyre, D.G. Zetaruk, X-ray photoelectron spectroscopic studies of iron oxides, Anal. Chem. 49 (2002) 1521–1529.

[57] K. Zhao, Z. Zhang, Y. Feng, S. Lin, H. Li, X. Gao, Surface oxygen vacancy modified Bi2MoO6/MIL-88B(Fe) heterostructure with enhanced spatial charge separation at the bulk & interface, Appl Catal B: Environ 268 (2020), 118740.

[58] F. Song, M.M. Busch, B. Lassalle-Kaiser, C.S. Hsu, E. Petkucheva, M. Bensimon, H. M. Chen, C. Corminboeuf, X. Hu, An Unconventional Iron Nickel Catalyst for the Oxygen Evolution Reaction, ACS Cent. Sci. 5 (2019) 558–568.

[59] F. Dionigi, Z.H. Zeng, I. Sinev, T. Merzdorf, S. Deshpande, M.B. Lopez, S. Kunze, I. Zegkinoglou, H. Sarodnik, D.X. Fan, A. Bergmann, J. Drnec, J.F. de Araujo, M. Gliech, D. Teschner, J. Zhu, W.X. Li, J. Greeley, B.R. Cuenya, P. Strasser, In-situ structure and catalytic mechanism of NiFe and CoFe layered double hydroxides during oxygen evolution, Nat. Commun. 11 (2020) 2522.

[60] C. Tang, H.F. Wang, X. Chen, B.Q. Li, T.Z. Hou, B. Zhang, Q. Zhang, M.M. Titirici, F. Wei, Topological Defects in Metal-Free Nanocarbon for Oxygen Electrocatalysis, Adv. Mater. 28 (2016) 6845–6851.

[61] S. Yasuda, L. Yu, J. Kim, K. Murakoshi, Selective nitrogen doping in graphene for oxygen reduction reactions, Chem. Commun. 49 (2013) 9627–9629.

[62] L. Yao, N. Zhang, Y. Wang, Y. Ni, D. Yan, C. Hu, Facile formation of 2D Co2P@ Co3O4 microsheets through in-situ toptactic conversion and surface corrosion: Bifunctional electrocatalysts towards overall water splitting, J. Power Sources 374 (2018) 142–148.

[63] M. Arif, G. Yasin, M. Shakeel, M.A. Mushtaq, W. Ye, X. Fang, S. Ji, D. Yan, Highly active sites of NiVB nanoparticles dispersed onto graphene nanosheets towards efficient and pH-universal overall water splitting, J Energy Chem 58 (2021) 237–246.

[64] Y.P. Zhu, Y.P. Liu, T.Z. Ren, Z.Y. Yuan, Self-Supported Cobalt Phosphide Mesoporous Nanorod Arrays: A Flexible and Bifunctional Electrode for Highly Active Electrocatalytic Water Reduction and Oxidation, Adv. Funct. Mater. 25 (2015) 7337–7347.

[65] K. Zhou, W.J. Zhou, X.J. Liu, Y. Wang, J.Q. Wan, S.W. Chen, Nitrogen Self-Doped Porous Carbon from Surplus Sludge as Metal-Free Electrocatalysts for Oxygen Reduction Reactions, Acs Appl Mater Inter 6 (2014) 14911–14918.

[66] M. Liu, K.A. Min, B. Han, L.Y.S. Lee, Interfacing or Doping? Role of Ce in Highly Promoted Water Oxidation of NiFe-Layered Double Hydroxide, Adv. Energy Mater 11 (2021) 2101281.

[67] X. Liu, J. Meng, J. Zhu, M. Huang, B. Wen, R. Guo, L. Mai, Comprehensive Understandings into Complete Reconstruction of Precatalysts: Synthesis, Applications, and Characterizations, Adv Mater 33 (2021) 2007344.

[68] J.F. Zhang, J.Y. Liu, L.F. Xi, Y.F. Yu, N. Chen, S.H. Sun, W.C. Wang, K.M. Lange, B. Zhang, Single-Atom Au/NiFe Layered Double Hydroxide Electrocatalyst: Probing the Origin of Activity for Oxygen Evolution Reaction, J. Am. Chem. Soc. 140 (2018) 3876–3879.

[69] O. Diaz-Morales, D. Ferrus-Suspedra, M.T.M. Koper, The importance of nickel oxyhydroxide deprotonation on its activity towards electrochemical water oxidation, Chem. Sci. 7 (2016) 2639–2645.

[70] K. Juodkazis, J. Juodkazytė, R. Vilkauskaitė, V. Jasulaitienė, Nickel surface anodic oxidation and electrocatalysis of oxygen evolution, J. Solid State Electrochem. 12 (2008) 1469–1479.

[71] L. Bai, S. Lee, X. Hu, Spectroscopic and Electrokinetic Evidence for a Bifunctional Mechanism of the Oxygen Evolution Reaction, Angew. Chem. Int. Ed. 60 (2021) 3095–3103.

[72] J. Chen, F. Zheng, S.-J. Zhang, A. Fisher, Y. Zhou, Z. Wang, Y. Li, B.-B. Xu, J.-T. Li, S.-G. Sun, Interfacial Interaction between FeOOH and Ni-Fe LDH to Modulate the Local Electronic Structure for Enhanced OER Electrocatalysis, ACS Catal. 8 (2018) 11342–11351.

[73] M. Kuang, J. Zhang, D. Liu, H. Tan, K.N. Dinh, L. Yang, H. Ren, W. Huang, W. Fang, J. Yao, X. Hao, J. Xu, C. Liu, L. Song, B. Liu, Q. Yan, Amorphous/Crystalline Heterostructured Cobalt-Vanadium-Iron (Oxy)hydroxides for Highly Efficient Oxygen Evolution Reaction, Adv. Energy Mater. 10 (2020) 2002215.

[74] X. Lu, C. Zhao, Electrodeposition of hierarchically structured three-dimensional nickel-iron electrodes for efficient oxygen evolution at high current densities, Nat. Commun. 6 (2015) 6616.

[75] C. Kuai, Y. Zhang, D. Wu, D. Sokaras, L. Mu, S. Spence, D. Nordlund, F. Lin, X.-W. Du, Fully Oxidized Ni–Fe Layered Double Hydroxide with 100% Exposed Active Sites for Catalyzing Oxygen Evolution Reaction, ACS Catal. 9 (2019) 6027–6032.

[76] S. Chen, Z. Kang, X. Zhang, J. Xie, H. Wang, W. Shao, X. Zheng, W. Yan, B. Pan, Y. Xie, Highly Active Fe Sites in Ultrathin Pyrrhotite Fe7S8 Nanosheets Realizing Efficient Electrocatalytic Oxygen Evolution, ACS Cent. Sci. 3 (2017) 1221–1227.

[77] Z. Cai, P. Wang, J. Zhang, A. Chen, J. Zhang, Y. Yan, X. Wang, Reinforced Layered Double Hydroxide Oxygen-Evolution Electrocatalysts: A Polyoxometallic Acid Wet-Etching Approach and Synergistic Mechanism, Adv. Mater. 34 (2022) e2110696.

[78] Z. He, J. Zhang, Z. Gong, H. Lei, D. Zhou, N. Zhang, W. Mai, S. Zhao, Y. Chen, Activating lattice oxygen in NiFe-based (oxy)hydroxide for water electrolysis, Nat. Commun. 13 (2022) 2191.

[79] N. Yu, W. Cao, M. Huttula, Y. Kayser, P. Hoenicke, B. Beckhoff, F. Lai, R. Dong, H. Sun, B. Geng, Fabrication of FeNi hydroxides double-shell nanotube arrays with enhanced performance for oxygen evolution reaction, Appl Catal B: Environ 261 (2020), 118193.

[80] C. Zhou, X. Chen, S. Liu, Y. Han, H. Meng, Q. Jiang, S. Zhao, F. Wei, J. Sun, T. Tan, R. Zhang, Superdurable Bifunctional Oxygen Electrocatalyst for High-Performance Zinc-Air Batteries, J. Am. Chem. Soc. 144 (2022) 2694–2704.

[81] D. Yan, Y. Li, J. Huo, R. Chen, L. Dai, S. Wang, Defect Chemistry of Nonprecious-Metal Electrocatalysts for Oxygen Reactions, Adv. Mater. 29 (2017) 1606459.

[82] A. Grimaud, O. Diaz-Morales, B. Han, W.T. Hong, Y.L. Lee, L. Giordano, K. A. Stoerzinger, M.T.M. Koper, Y. Shao-Horn, Activating lattice oxygen redox reactions in metal oxides to catalyse oxygen evolution, Nat. Chem. 9 (2017) 457–465.

[83] J. Yin, Y. Li, F. Lv, M. Lu, K. Sun, W. Wang, L. Wang, F. Cheng, Y. Li, P. Xi, S. Guo, Oxygen Vacancies Dominated NiS2/CoS2 Interface Porous Nanowires for Portable Zn-Air Batteries Driven Water Splitting Devices, Adv. Mater. 29 (2017) 1704681.

[84] X. Lu, G. Wang, T. Zhai, M. Yu, J. Gan, Y. Tong, Y. Li, Hydrogenated TiO2 nanotube arrays for supercapacitors, Nano Lett. 12 (2012) 1690–1696.